WWU
MÜNSTER

KATRIN
KARLSRUHE TRITIUM NEUTRINO EXPERIMENT

› Designing and optimizing the UV illumination of the rear wall at the KATRIN experiment by simulation

Bachelor thesis
Benedikt Bieringer

Referent: Prof. Dr. C. Weinheimer
Korreferent: Prof. Dr. rer. nat. Dr. h.c. E. Otten

Westfälische Wilhelms-Universität Münster
Institut für Kernphysik
AG Prof. Dr. C. Weinheimer

Münster, November 2017

living.knowledge

Declaration of Academic Integrity[1]

I hereby confirm that this thesis on "Designing and optimizing the UV illumination of the rear wall at the KATRIN experiment by simulation" is solely my own work and that I have used no sources or aids other than the ones stated. All passages in my thesis for which other sources, including electronic media, have been used, be it direct quotes or content references, have been acknowledged as such and the sources cited.

_____

(date and signature of student)

I agree to have my thesis checked in order to rule out potential similarities with other works and to have my thesis stored in a database for this purpose.

_____

(date and signature of student)

[1] As found on `https://www.uni-muenster.de/imperia/md/content/math_nat_fakultaet/pruefungsamt/pruefungsamt_neu/allgemein/plagiatserkl__rung_englisch.docx`

Contents

1 Introduction

In this thesis, an optical system design for the experiment KATRIN is presented and optimized.

The goal of the Karlsruhe Tritium Neutrino (KATRIN) experiment is to determine the electron antineutrino mass by precisely measuring a tritium β^- decay electron spectrum. This decay produces $^3\mathrm{He}^+$, an electron and the electron antineutrino $\bar{\nu}_e$. In general, single β^- decays can be described as

$$n \rightarrow p + e^- + \bar{\nu}_e \,. \tag{1.1}$$

Conservation of energy implies that the electron energy spectrum endpoint depends directly on the mass of the electron antineutrino. Therefore a precise measurement of this endpoint is crucial for the determination of an upper limit for the electron antineutrino mass.

Figure 1.1 shows the general setup of KATRIN. The windowless gaseous tritium source (WGTS), which is filled with gaseous tritium (T_2), provides the measured electron flux which is guided on magnetic flux lines through the transport section. In this section the tritium flow (in mbar) is reduced by a factor of about 10^{14} [2, p. 31]. The guidance is achieved by deflection of the electrons into spiral traces by the magnetic field. In the following MAC-E-Filters, the pre- and main spectrometer, the electrons are collimated by adiabatic attenuation of the guiding magnetic field and then filtered using an electrostatic field. The decrease of the magnetic field also decreases the momentum $p_\perp^2$ orthogonal to the magnetic flux lines and therefore changes their direction towards the magnetic flux lines. This is theoretically described as conservation of the relativistic factor γ and the magnetic moment μ, also expressable via the magnetizing force B of the surrounding magnetic field: [3, eq. 3]

$$\gamma\mu = \frac{p_\perp^2}{B} = \text{const.} \tag{1.2}$$

As a result, the momentums of all electrons are mostly oriented forwards and an electrostatic field can be used as an energy filter, which is then a MAC-E-Filter. The energy resolution of this filter $\Delta E/E$ is given by

$$\frac{\Delta E}{E} = \frac{B_\mathrm{min}}{B_\mathrm{max}} \tag{1.3}$$

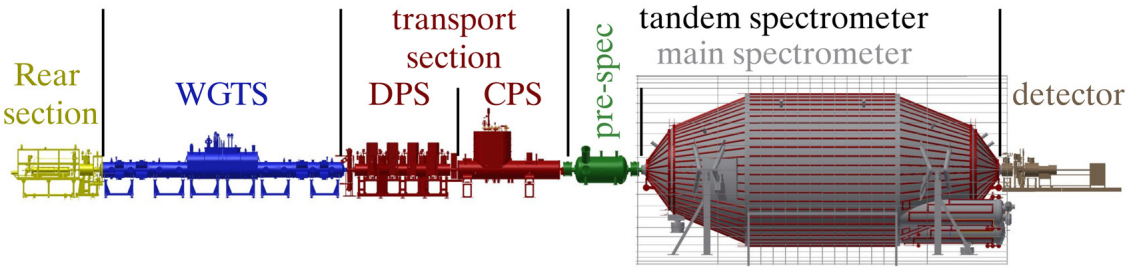

Figure 1.1: Overview of the KATRIN experimental setup [1, p. 32, fig. 2.5]. The rear section is part of the Calibration and Monitoring System (CMS) and contains the rear wall chamber. The windowless gaseous tritium source (WGTS) is filled with the tritium of which the decay is analyzed. The following transport section is composed of the Differential Pumping Section (DPS) and the Cryogenic Pumping Section (CPS), both guide the electrons emitted from tritium β^--decay to the pre-spectrometer and reduce the tritium flux towards the spectrometers. The first part of the tandem spectrometer is the pre-spectrometer (pre-spec), which reduces background electrons for the following main spectrometer. Second, the main spectrometer reduces the electron flow for all electrons below an adjustable treshold. The residual electrons are then collected in the detector.

where B_{min} is the magnetic field in the analyzing plane of the filter and B_{max} is the magnetic field in the WGTS. The energy resolution of the main spectrometer is $\Delta E = 0.93\,\text{eV}$ for an energy of $E = 18.5\,\text{keV}$. Via measurement of the electon time of flight, an even finer resolution can be achieved. This leads to an upper neutrino mass limit of at least $0.2\,\text{eV}$ [4].

The decaying tritium produces a charged plasma in the WGTS with a high conductivity along the magnetic flux lines and a low conductivity in the magnetically confined directions [5, p. 167 and sec. 5.3.4.1]. In the rear section all magnetic flux lines pass a golden, circular wall, the rear wall, meaning the wall sets the electric potential of the plasma [6, p. 10]. This wall, therefore, describes one end of the electron guidance of KATRIN. It is located inside the rear wall chamber, a vessel directly connected to the WGTS. Because the source emits electrons, the gas inside the WGTS is positively charged and therefore attracts other emitted electrons. Inducing electrons into the plasma by illuminating UV radiation onto the rear wall compensates this effect [7, pp. 223 sqq.].

The UV radiation is emitted from a xenon short-arc lamp with a parabolic mirror. It is then widened with a refracting telescope to match the specified width of the rear wall, as presented in chapter 2. The aim of this work is to improve the layout of the telescope by simulations introduced in chapter 3 and evaluated in chapter 5 to match the required specifications such as an illumination power of at least 200 mW and a diameter of the illuminated rear wall surface of at least 140 mm.

2 Current design of the rear wall illumination

The UV illumination is produced by a xenon short-arc lamp with an emission spectrum wider than 1 μm. This spectrum is cut off by two dichroic beam splitters used as low pass filters by reflecting only rays with a wavelength below e.g. 266 nm. The count of two beam splitters was chosen to sharpen their overall reflection selectivity. The resulting UV light in a wavelength range from 200 to 266 nm is then passed through two lenses that work as a refracting telescope. This telescope type focusses the incoming light on a common focus of two lenses. Behind the second lens, the viewer is positioned. For this system, the telescope is designed to widen a parallel beam to the radius of the homogeneous ray bundle of 140 mm. The described setup is displayed in figure 2.1, which introduces parameters for the optical setup. The rear wall itself is positioned behind the second lens and centered to the optical axis. Its normal vector and the optical axis enclose 54°.

The following subsection explaines the Cermax-Box housing of the lamp and the two dichroic beam splitters. It is followed by the explanation of the telescope lens system.

The design as shown in this chapter has been proposed and elaborated by E. Otten.

2.1 Cermax-Box

The fundamental setup of the Cermax-Box is shown in figure 2.2. It contains the Excelitas Cermax PE1000DUV xenon short-arc lamp as source of parallelized light, which will from now on be referred to as *Cermax lamp* or *lamp*. The lamp consumes a power of 1000 W with a radiant output of 250 W of which approx. 2.10 W are under 266 nm and 1.74 W are under 260 nm. This has been determined by comparing the area under the lamps light spectrum from 200 to 260/266 W and to 390 W. For the last one a power of 25 W is specified [8, p. 12]. The emitted spectrum can be seen in figure 2.3. Wavelengths under 266 nm are reflected by the following two dichroic beamsplitters. The remaining radiation is transmitted on oil or water cooled beam dumps.

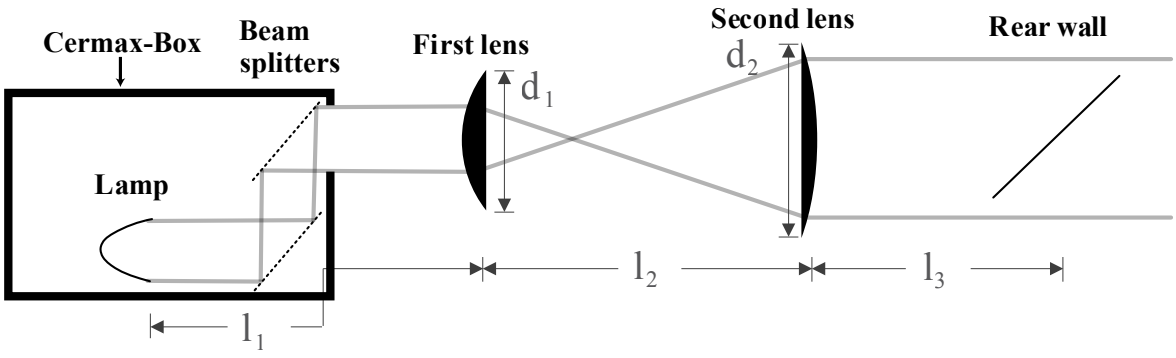

Figure 2.1: The studied lens system. Introduced parameters are the distance between lamp opening and the first lens l_1, the distance between both lenses l_2, the distance between the second lens and the rear wall l_3, the diameter of the first lens d_1 and the diameter of the second lens d_2. The Cermax-Box surrounds Cermax lamp and beam splitters.

2.2 Lens system

The lens system including the environmental setup can be seen in figure 2.4. Both lenses are single piece fused silica lenses with antireflective coating. The first lens is supposed to generate a focal point near the quartz window which passes the light from inside the second containment to inside the first containment.[1] The second lens is held by a casting attached to the inner Rear Section vacuum chamber and positioned between a window and the rear wall. Through this window the beam is passed onto the second lens.

The distance between the two lenses l_2 is for perfect, superflat lenses the sum of the lenses focal lengths $f_1 + f_2$. The intercept theorem provides the following relation:

$$\frac{r_1}{f_1} = \frac{r_2}{f_2}\,. \tag{2.1}$$

Here r_1 and r_2 are the radii of the parallel beam bundle passing the first and the second lens.

One can use the optical property *étendue* ξ to prove that for lenses without aberration smaller focal lengths of the first lens result in smaller ray distributions in its focal point: The étendue, also called "acceptance", is defined as [10][11]

$$\xi = n^2 \iint\limits_{\text{apertures}} \cos\theta \,\mathrm{d}A_\mathrm{s}\,\mathrm{d}\Omega \tag{2.2}$$

[1] Containments are layered enclosures for the tritium. The inner enclosure is called "first containment", the outer is called "second containment".

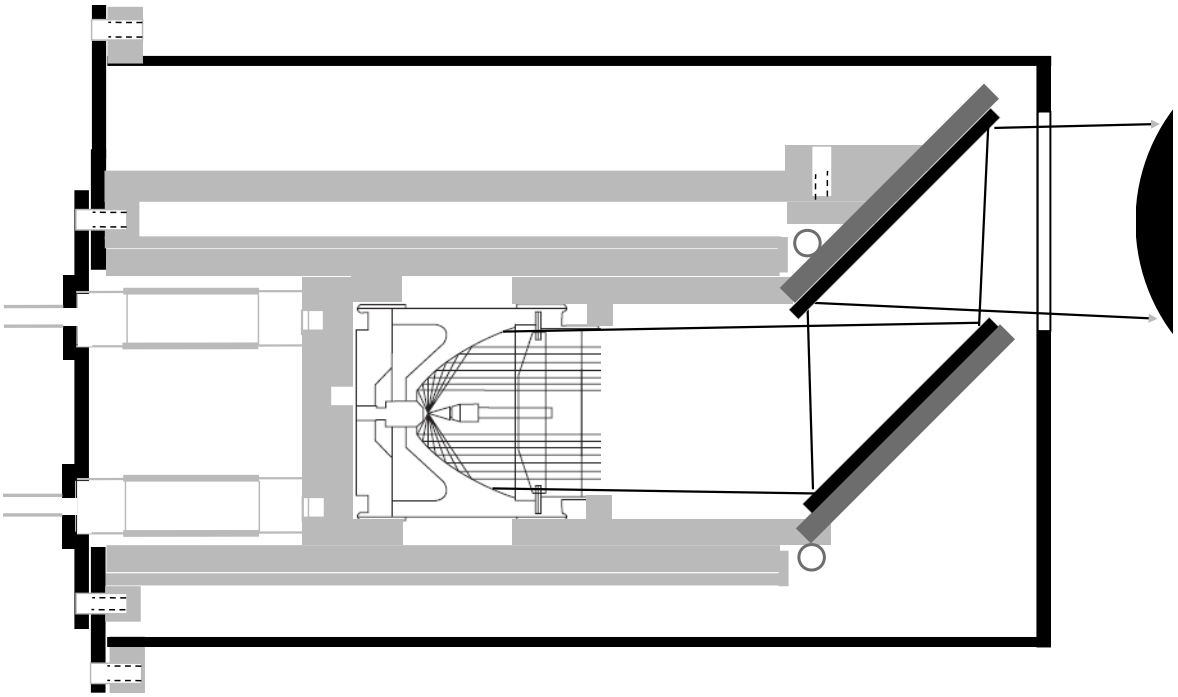

Figure 2.2: Technical drawing of the Cermax-Box. The enclosure, the beam splitters and the first lens are black, its cooling and the beam dumps are dark grey and other components are light gray. The schematic cross section of the lamp is taken from [9, p. 3, fig. 2(b)]. *Adapted from E. Otten, unpublished.*

and describes the relation between the spatial ray distribution on an arbitrarily located exit aperture from an entrance aperture. The index of refraction is n, the incidence angle is θ, the corresponding infinitessimal entrance aperture element is $\mathrm{d}A_\mathrm{s}$ and the exit aperture element is $\mathrm{d}\Omega$.

Since the étendue is conserved, one can derive the relation of the first lenses focal length to the size of the ray distribution in its focal plane: The entrance aperture is placed to the first lens and the exit aperture to the focal point. The shorter the considered focal length is, the larger is the average incidence angle on the exit aperture. Conservation of étendue results in a smaller beam cross section in the focal plane and therefore the second lens is illuminated from a smaller distribution in the focal point.

In this work plano-convex spherical lenses are used. The planar side of both lenses is oriented towards the focal point to which the beam is concentrated. Because the second lens is considered to be inside the rear wall chamber, its surrounding limits its maximum size to 155 mm.

The lenses consist of fused silica. Its refractive index and the extent of the lens surface not only cause spherical aberrations, but also a shift of the focal point. Principal planes can be constructed for each lens side, the front (1) and the back (2). Their distance is given as

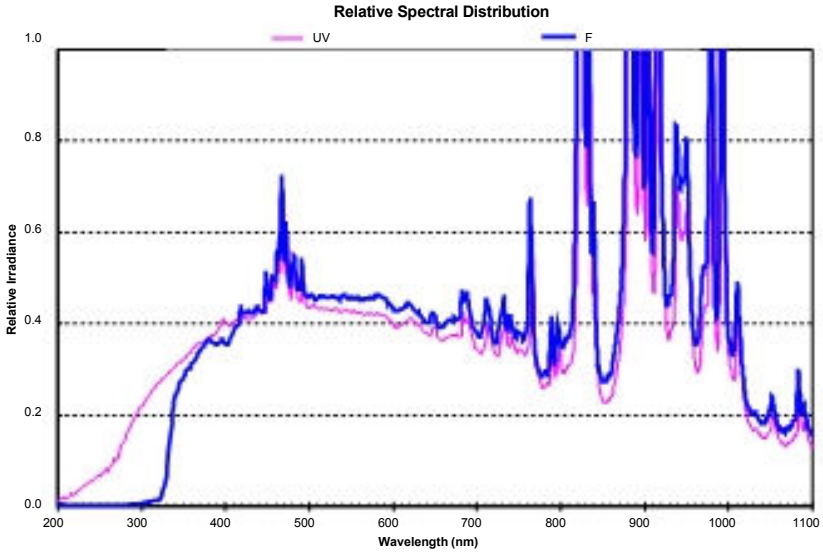

Figure 2.3: Relative spectral distribution of the Cermax lamp output [8, p. 12]. The y-axis has been replaced to improve the readability.

distances h_1 and h_2 from the furthest part of the lens surface at the regarding side towards the middle of the lens.[12]

Approaching the refractive index of air with 1, the following formula describes the distance $h_{1/2}$:

$$h_{1/2} = \frac{f(n_\mathrm{l} - 1)d}{R_{2/1} n_\mathrm{l}} \text{ [12, 13]}, \tag{2.3}$$

where n_l is the refractive index of the lens material, d is the thickness of the whole lens[2], f is the focal length of the lens and $R_{2/1}$ the surface curvature of the respecting side.

The lens parameters can be determined via the equation for effective focal lengths [12, p. 397]:

$$\frac{1}{f} = (n-1)\left(\frac{1}{R_1} - \frac{1}{R_2}\right) + \frac{(n-1)d}{nR_1R_2}\,, \tag{2.4}$$

where f is the focal length of the lens, d its thickness, n the refractive index of the lens material, n_0 the refractive index of the surrounding medium and R_1 and R_2 the lenses radii of curvature. In this case, R_2 is infinitely large as one side of the lens is planar. Hence the equation (2.4) is in this case simplified to

$$f = \frac{1}{n-1} R_1\,. \tag{2.5}$$

[2] d is the distance between each sides furthest part of the lens surface measured from the lens center.

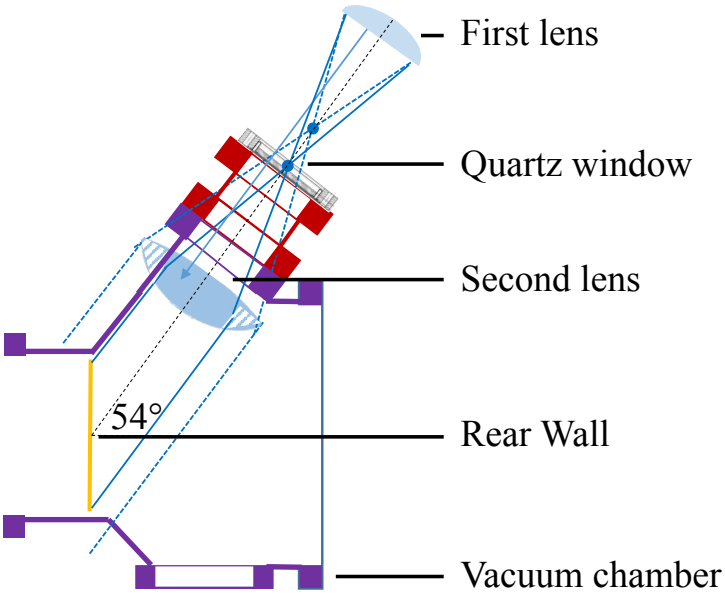

Figure 2.4: Annotated side view on the lens system in its surrounding setting. The Cermax-Box is outside the figure in its top right corner. The ruled area of the second lens is cut off because of geometrical boundary conditions. *Adapted from E. Otten, unpublished.*

3 Simulation implementation of the illumination system

The following chapter describes the implementation of the rear wall illumination in simulations. First, general information on the used software and procedure is given. The 2d simulation setting is then introduced. After that, the differences between the 2d and the 3d simulation, which can be seen as an extension of the 2d simulation, are explained. As the simulation implementation varies for the simulation of spherical aberrations, it is then presented in a further subchapter.

All simulations presented in the following two subchapters have been done with COMSOL Multiphysics® [14] and the corresponding ray optics module, abbreviated as *COMSOL*. The COMSOL internal Application Builder was used to automatize the simulation and the aquired data was processed with custom Python [15] scripts using SciPy [16].

COMSOL simulates the optical setting by discretizing the setting into a mesh and then reducing the simulation time steps until a convergent solution for a generated set of rays is found. Tolerances specify in which dimension a convergent solution has to be found.

As a mesh resolution, the default physics-controlled mesh in a size of "extremely fine" is chosen. Typically, the following simulations are done with a ray count of 10^5. Some simulations also have a ray count of 10^6. The COMSOL simulation step size is automatically adjusted until the wave vectors and ray position converge inside a relative tolerance of 10^{-5} of each value. For realistic ray trajectories time steps of 0.1 ns are used.

For the following simulations a wavelength of 225 nm is used if not specified otherwise. Simulations with wavelengths of 200 and 260 nm are discussed in section 4.7.

3.1 2d simulation in COMSOL

To simulate the given optical setting in 2d, its different components are integrated into the simulation step by step. After the mirrors are discussed, two light source models are reviewed,

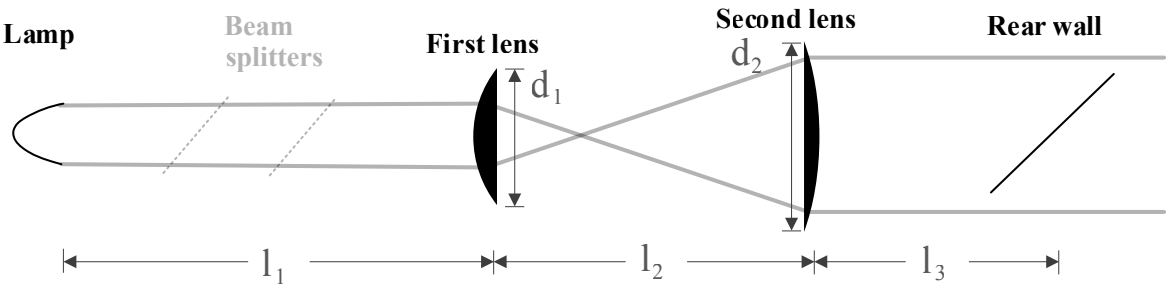

Figure 3.1: The axisymmetric simplification of the studied lens system. In comparison to figure 2.1, the Cermax-Box housing is not marked and the two mirrors no longer reflect light. Instead the beam path behind the mirrors is moved so that all optical components shares the same optical axis.

which are a point source and a Gaussian emitter. The lamp contains anode and cathode, which also have to be modeled. Finally, the lens implementation will be covered.

3.1.1 Mirrors

The optical setting itself as shown in figure 2.1 contains the parabolic mirror and the two beamsplitters that mirror the investigated UV radiation between 200 and approx. 260 nm. As the simulations are done with one wavelength at a time and only the relative ray count is analyzed, the beam splitters' lowpass effect is not relevant for these simulations and can therefore be ignored. Mirrors only influence the direction of axisymmetric ray bundles, so they do not change the angular or spacial ray distribution. Since the average direction of the ray bundle exiting the Cermax-Box is known, including the mirrors into the simulation does neither enhance the simulation accuracy nor bring new insight. Therefore the optical setting can be reduced to the axisymmetric setting shown in figure 3.1.

The parabolic mirror is characterized in the lamp specifications [8, p. 12] as shown in figure 3.2. This figure gives the equation

$$\mathrm{Y}^2 = 0.8\mathrm{X} \tag{3.1}$$

and the lengths R and F. From this information, it can be inferred that the parabola is proportional to a parametrization of

$$f(x) = \frac{1}{0.8} \cdot x^2 \tag{3.2}$$

for a maximum $f(x) = \mathrm{F} + \mathrm{R} = 1.250$. Therefore x is in range $[-\sqrt{0.8 \cdot 1.25}, \sqrt{0.8 \cdot 1.25}]$ which gives a diameter of the aperture in this parametrization of $2 \cdot \sqrt{0.8 \cdot 1.25}$. The technical

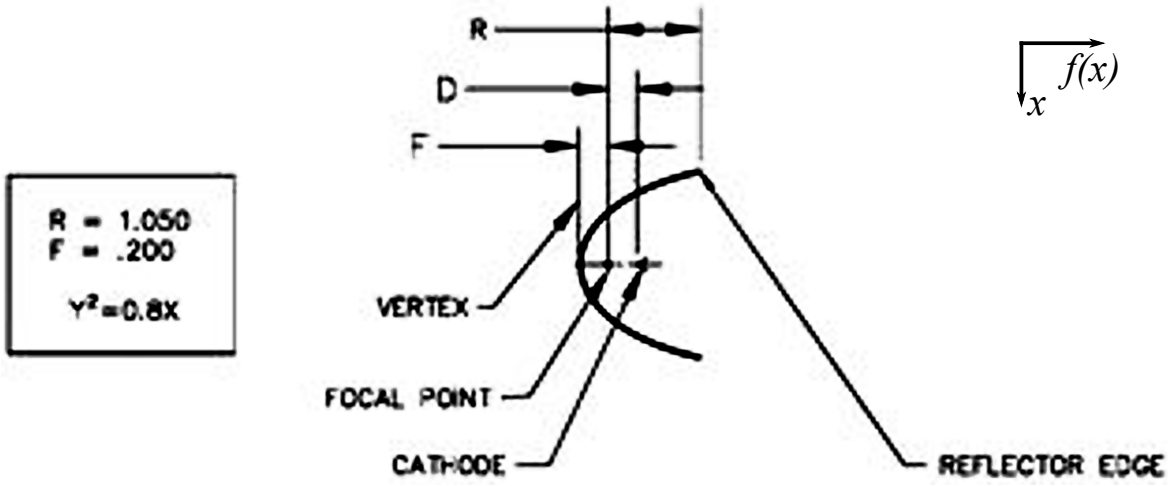

Figure 3.2: Parabolic parametrization as specified for the lamp [8, p. 12]. A cross section of the lamp is shown and different lengths are introduced. The equation $Y^2 = 0.8\,X$ and the height of the paraboloid of F+R= 1250 are given for its parametrization. Edited for better readability, added coordinate axes.

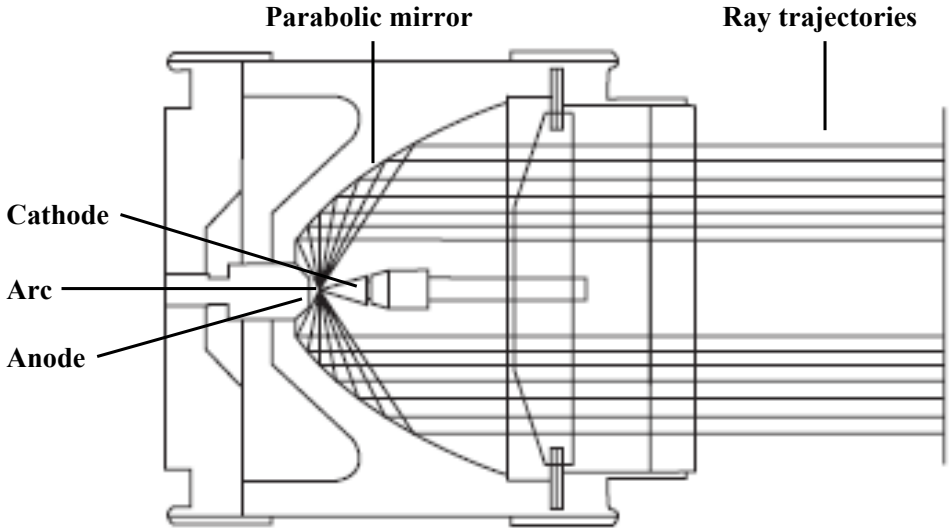

Figure 3.3: Schematic cross section of the Cermax lamp [9, p. 3, fig. 2(b)], with additional labels. From the guides characterization of lamp LX1000CF it can be reasoned to be an alternative name of the lamp PE1000DF which has the same inner structure as the regarded lamp PE1000DUV. Therefore this figure can be used for PE1000DUV, although it is annotated only with LX1000CF.

drawing from figure 3.3 shows, that the window diameter of 50.8 mm is also the size of the aperture of the parabolic mirror, at least up to the given resolution of the figure. Therefore the given parametrization has a scaling factor of $50.8\,\mathrm{mm}/(2 \cdot \sqrt{0.8 \cdot 1.25}) = 25.4\,\mathrm{mm}$ in both directions. The distance of the parabola's focal point to its bottom of F= 0.200 also has to be scaled with this factor.

3.1.2 Point source

The simplest approximation to the light source is a point source in the calculated focal point of the parabola. This can be used for a sanity check of the implemented parabolic mirror or future lenses. The results of these simulations do not represent the angular distribution of outcoming rays, because rays emitted from a parabola's focal point and mirrored by the parabola are perfectly parallel [17].

The angular distribution of this point source cannot be isotropic, because the 2d simulation is the equivalent of an infinitessimal cylindrical sector of the 3d simulation along the optical axis and therefore its rotational extrusion has to be similar to the respective 3d simulation. If the distribution was isotropic, its extrusion would have an infinitely high intensity in axial direction and an infinitely low intensity in radial direction. If the distribution has an intensity proportional to $\sin(\alpha)$ for the angle α, defined such that $\alpha = 0$ and $\alpha = \pi$ lay on the opticla axis, its extrusion has a isotropic angular distribution. This can be shown by assuming that all rays are emitted from a point source without additional optical geometry around them and have passed a specific length a. They then all lie on a spherical surface with a radius of a. If one then selects a rotational symmetric, connected, infinitessimal area with a width of $\mathrm{d}x$ on this sphere, its area is $2\,\pi\,r\,\mathrm{d}x$, where r is the radius of a circle. All rays laying on this circle are emitted with the same angle α, giving $r = \sin(\alpha) \cdot a$. If one normalizes the infinitesimal intensity emitted in this direction to its infinitesimal area, the result is independent of the angle. Therefore the angular distribution is weighted correctly.

3.1.3 Gaussian emitter

To achieve a more realistic angular ray distribution, the extent of the source, the "short arc", has to be considered. This is done by assuming a Gaussian distribution of point emitters, each emitting a single ray in a pseudo-random direction. A Gaussian distribution has a spatial weight of

$$f(x) \propto \exp\left(-\frac{x^2 + y^2 + z^2}{2\sigma^2}\right), \tag{3.3}$$

where x, y and z are the spatial coordinates and σ is the standard deviation.

From plausibility considerations, a value of σ between 0.5 and 1 mm is assumed for these simulations. The COMSOL specific "position refinement factor" is set to its default value of 0, as the resulting lower accuracy in the source distribution primarely widens the angular distribution of the rays exiting the lamp and can therefore be compensated by choosing $\sigma = 0.5\,\text{mm}$. A circle with a radius of 2 mm is chosen as a boundary for the emitter. Because rays in the real 3d setting are not necessarily only emitted in radial directions, the 2d simulation cannot be expected to generate a realistic angular distribution, which will be later discussed for the axisymmetric 3d simulation. Also the angular distribution of ray directions presented in the last subchapter only applies for sources on the optical axis. Since the Gaussian distributed single-ray emitters do not lay on the optical axis except for an infinitessimal amount, the angular distribution has to be corrected for each emitter individually. Another approach to this problem is a 3d simulation. In the presented simulations, the angular weight of the point source is also used as an approximation for the Gaussian emitter.

3.1.4 Lamp-internal anode and cathode

The emitter itself is surrounded by anode and cathode, which ensure the required power supply. They have to be included into the simulation because they dump beams. The dimensions and position of both are not documented and have to be estimated from figure 3.3. The blinds can be simplified and modelled in 2d as two lines which delete rays passing it. The first line is estimated to be at a height of $7.6 \cdot 10^{-4}\,\text{m}$ above the bottom of the parabola with a width of 7.8 mm. The second line is estimated to be at a height of 14 mm with a width of 6 mm.

3.1.5 Lenses

The lenses consist of fused silica of which the refractive index for the considered wavelength is $n = 1.5242$ [18]. For simulations with a wavelength of 200 nm, the refractive index it is $n = 1.550$ [19], for a wavelength of 260 nm it is $n = 1.5024$. Distances including one or both lenses are calculated from the correspondent primary planes. Rays reflected by lenses are not allowed as for every lens surface in the final setup an antireflective coating will be used. As this coating is not perfect for every angle of incidence, this will cause power losses that are not yet considered.

3.2 3d simulation in COMSOL

In this section, the 3d simulation is discussed, first as axisymmetric setting and then for the rear wall with non-axisymmetric results. As already emphasized, the 2d simulation cannot include rays of which its direction and the optical axis are skew. Furthermore, for a correct directional angular distribution of the rays, the ray emission angles had to be weighted dependent on the emitter position. Therefore, to cover more ray paths and for a simple achievement of a correct angular distribution, a 3d simulation is important. This 3d simulation can still be axisymmetric and can therefore be evaluated like its 2d equivalent.

3.2.1 Axisymmetric results

The step from 2d to 3d is a rotational extrusion of the 2d simulation around the optical axis. The 2d Gaussian distribution of the source emitted inside a circular boundary becomes a 3d Gaussian distribution emitted in a sphere of the same size. The angular distribution of the emission is pseudo-randomly generated by an arbitrary seed and as the setting is 3d, the distribution is unweighted.

To produce comparable results, the ray position is interpolated on specific plane surfaces, so-called *cuts*, in specific heights c on the optical axis, such as distances from the lenses or from the tip of the parabolic mirror. These cuts can then be plotted as radial-dependent histographs, where each bin has to be weighted with the area under which it collects rays in the cut. Therefore inner bins are weighted more than outer bins and outer bins have way better statistical results. Another approach weights each ray with an individual weight factor depending on its distance from the optical axis, but for randomly very small distances this creates very large weight factors and therefore influences the result more than in a bin-wise weighting. The used weight factor $w(r)$, which depends on the bin size b and the distance of a specific ray r, is the following:

$$w(r) = \frac{\pi b^2}{A(r)}, \text{ with} \tag{3.4}$$

$$A(r) = \pi \cdot (r_\mathrm{f}(r) + b)^2 - \pi \cdot r_\mathrm{f}(r)^2 \text{ and} \tag{3.5}$$

$$r_\mathrm{f}(r) = \left\lfloor \frac{r}{b} \right\rfloor \cdot b\,, \tag{3.6}$$

where $\lfloor \cdot \rfloor$ is the floor function, $A(r)$ the area under the specific bin and $r_\mathrm{f}(r)$ the discretized radius describing the smallest distance from the optical axis in the specific bin in which a ray with a distance of r from the optical axis is collected. This leads to the following *intensity distribution plots*.

Another used plot type of the ray trajectories cuts is an integration over the ray count dependent on the distance. This shows precisely, how many rays are outside or inside a specific range. Since this integration has not been binned or weighted, the resulting diagrams are also a lot smoother and have a much higher resolution than the histograms. This is used for an estimation of total intensities with which a circular surface is illuminated. This representation will be referred to as *integral plot*. The bin width of the shown integral plots is 1 mm.

Moreover, the ray trajectories cuts are used to calculate plots of the rays angular distribution. This is achieved by using the binning of the intensity distribution plot and calculating the respective angles to the bin borders. A distance of r from the optical axis at a cut at height of Z measured from ground of the parabolic mirror equals an angle β of $\beta = \tan^{-1}(r/z)$. The graphical representation of this processing will be called *angular distribution plot*.

3.2.2 Rear wall histograms

As the rear wall does not cut the ray bundle orthogonally, but in a plane with an angle of 54°, its illumination is not represented by one orthogonal ray trajectory cut, but by a theoretically infinitely large set of those. An alternative to the axisymmetric approach is a histogram plot of a real 2d cut at the position of the rear wall and then a histogram of the ray count on area elements on this rear wall. These plots do not use the axisymmetry of the simulation, so they need more simulated rays to get as much statistics per bin as the axisymmetric plots show.

3.3 Spherical aberration of plano-convex lenses

To get a better overview over the spherical aberration, an additional simulation is set up. As this simulation only consists out of a few fundamental calculations, it is entirely realized in Python. Rays emitted in a direction parallel to the optical axis and shining onto the spherical side of a plano-spherical lens are simulated. The point of interest is the position at which this ray crosses the optical axis. To compare this to the primary plane calculation, the distance between this point and the expected focal point determined using the primary plane image is calculated. In the resulting plot, these values are plotted against the initial distance of the rays to the optical axis before the incident on the lens. This is accomplished using Snell's law and trigonometric relations.

4 Illumination results and optimization

In this chapter the simulation results and their conclusions are presented and used to optimize the lamp system. This is done by analyzing the light path of the setup for each component. First, the parabolic mirror and lens internal blinds will be considered. Because these blinds are visible in optical images, their effect has then to be discussed. With the results from these considerations, a diameter of both lenses can be found. Then the distance between the two lenses is optimized. After regarding the spherical aberrations of the lenses, a defocusing of the second lens is used to widen the ray to illuminate the desired portion of the rear wall.

4.1 Parabolic mirror

A parabolic mirror itself causes an inhomogeneous ray bundle with a high ray count near the optical axis that falls off for higher distances. In figure 4.1, results of a 3d axisymmetric simulation with only the mirror and a point source are shown for a cut at the aperture of the paraboloid. In the real lamp, the blinds and the spatial extension of the arc take effect. In figure 4.1 the same cut is shown after adding both the Gaussian distributed source and the blinds. It can be seen, that in the near field of the lamp, the inhomogenity and the shadow from the blinds are still visible. The cut after 0.1 m in figure 4.2 in comparison to figure 4.1 shows the effect of the diverging rays caused by rays not emitted exactly from the lamps focal point.

From the ray trajectories directions, the angular distribution of the rays in the far field can be evaluated for a cut after 2.5 m to the results shown in figure 4.3. The distribution has a full width half maximum (FWHM) of $(4.0 \pm 0.3)\,^\circ$. Compared to the specifications of the Cermax lamp in figure 4.4 with an estimated FWHM of $(3.0 \pm 0.2)\,^\circ$, the divergence of the simulated ray bundle in the simulation is larger than the specified one. The uncertainty for the simulation result is derived from its binning and the uncertainty of the specificated distribution is given by the inaccuracy resulting from the extraction of data from a pixely plot. It is unclear whether this is an accurate comparison as it is not specified, in which distance from the lamp and how the “far field” angular distribution was measured. The difference between specified and real angular distribution can be accepted, because the source widens

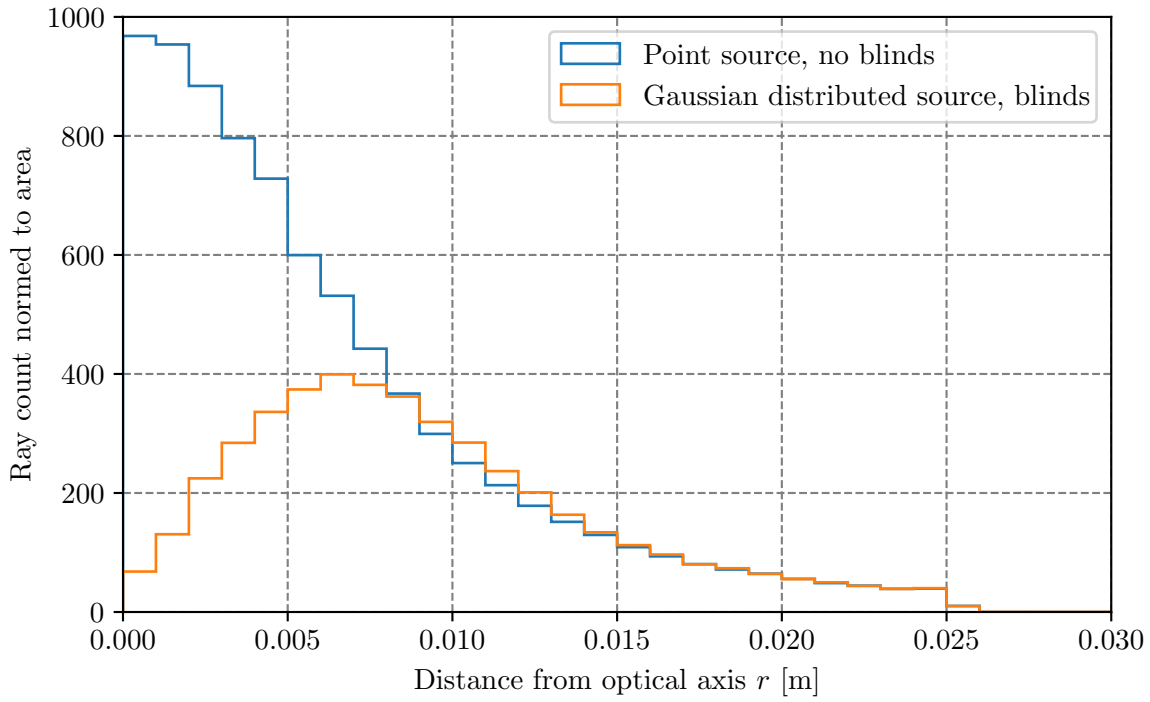

Figure 4.1: Intensity distribution plot at height of the paraboloid aperture. The distributions are shown for both a paraboloidic mirror with a point source in the mirrors focus without blinds and a Gaussian distributed source with $\sigma = 0.5\,\text{mm}$ with blinds.

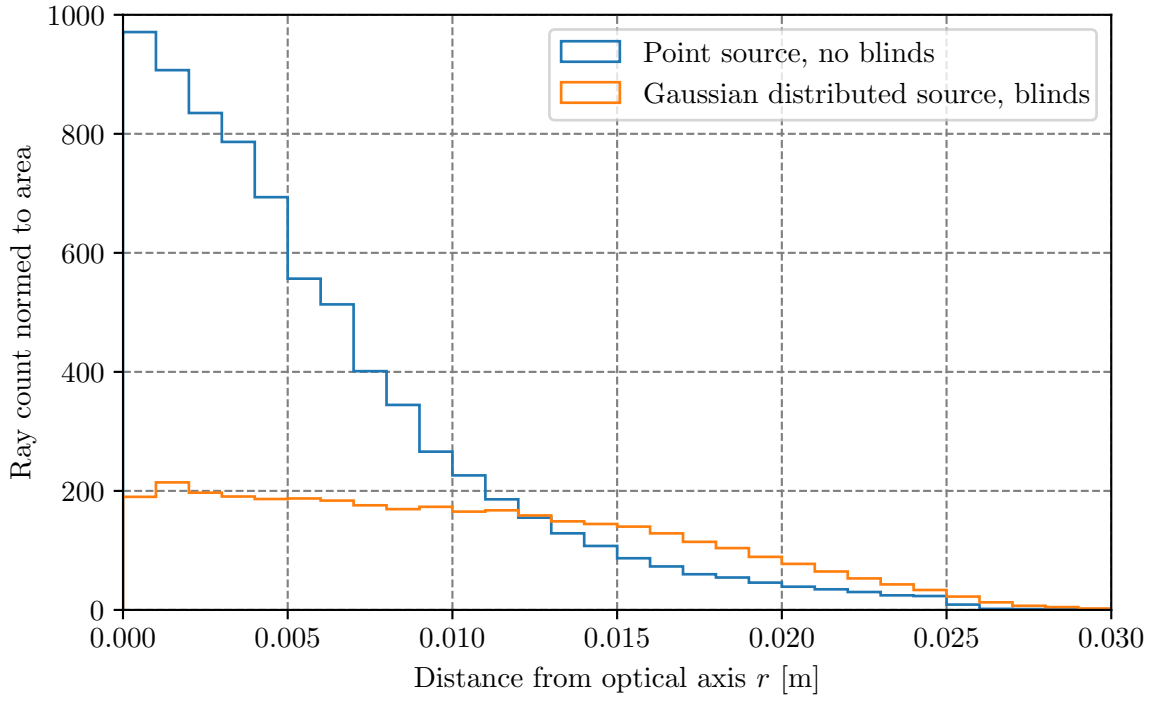

Figure 4.2: Intensity distribution plot at a distance of 100 mm before the paraboloid aperture. The distributions are shown for both a paraboloidic mirror with a point source in the mirrors focus without blinds and a Gaussian distributed source with $\sigma = 0.5\,\text{mm}$ with blinds.

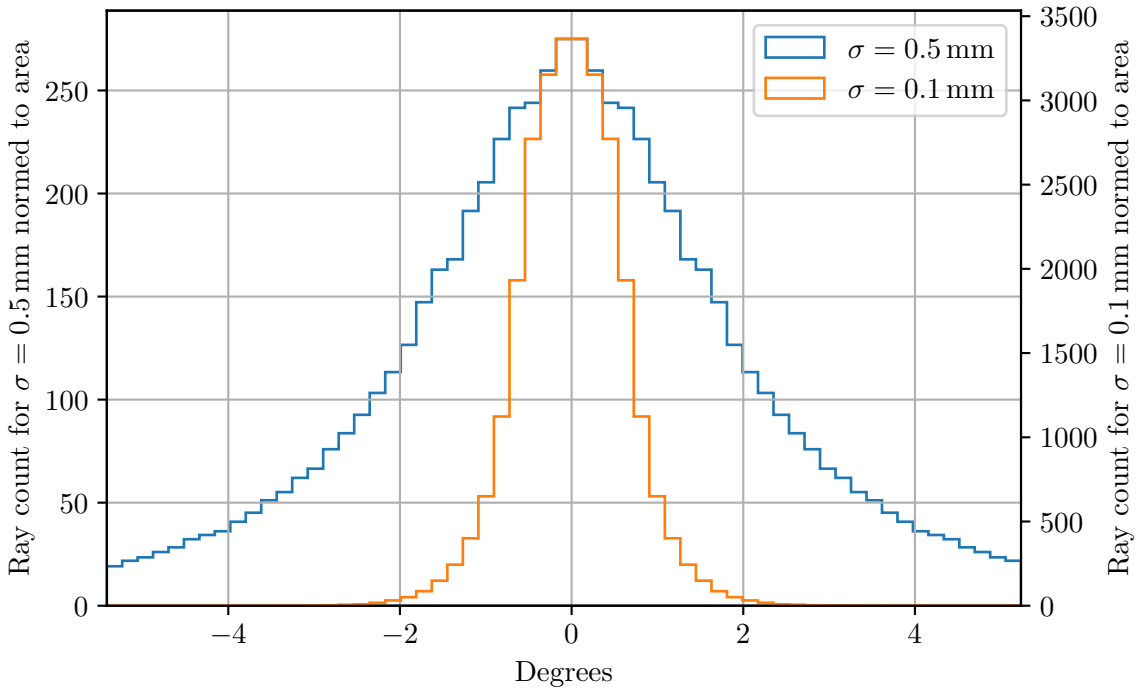

Figure 4.3: Angular distribution of the lamps far field 2.5 m behind the paraboloid aperture. The distributions are shown for both a Gaussian distributed source with $\sigma = 0.5\,\mathrm{mm}$ and with $\sigma = 0.25\,\mathrm{mm}$. Bin size: 8 mm radially in cut plane.

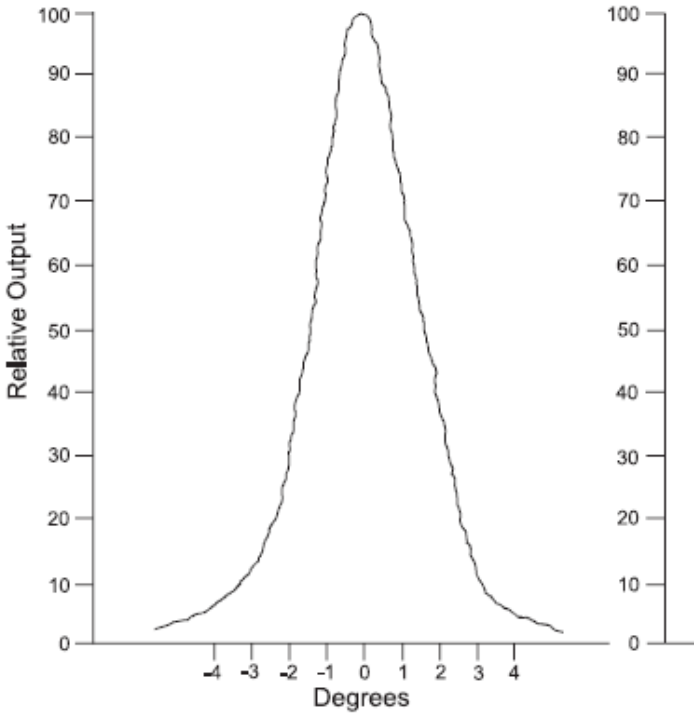

Figure 4.4: Beam shape of the lamps far field as shown in the engineering guide [9, p. 18, fig. 27]

over time and with a wider source the ray divergence rises. Therefore, simulating a lamp with a slightly higher divergence shows possible problems and is necessary. In figure 4.3 the result for a smaller source with $\sigma = 0.1\,\text{mm}$ can be seen. For this distribution, the mesh size of the emitter geometry is in the size of the emitter distribution which necessitates a "position refinement factor" (see chapter 3) of 1 to be used. As the exact arc geometry is not known well enough to implement it into the simulation, and the given distribution only applies for new lamps, a conservative σ of $\sigma = 0.5\,\text{mm}$ will be used.

4.2 Shadow

After adding an extent to the source, the blind spots created by the internal blinds of the lamp are covered and only visible in the near field. Nevertheless, they reappear in optical images as created by the telescope setup. This can be seen in figure 4.5, in which the ray trajectories of two 3d simulations are shown. It can be seen that depending on the distance of the optical setup from the lamp, a low radiation zone appears behind the second lens. This can be explained by optical imaging:

For an irradiated object that is positioned close enough in front of the first lens, an optical image of itself behind the second lens is produced. The blinds are imaged as black objects and consequently follow the laws of optical imaging. From the Gaussian Lens Formula [12, p. 267]

$$\frac{1}{o} + \frac{1}{i} = \frac{1}{f} \tag{4.1}$$

for object size o, image size i and focal length f, it can be derived that the minimal distance necessary to image the object/shadow is equal to the focal length of the first lens f_1. To show this, the distance between the thin lens 1 and the object is called o_1, the image created by lens 1 with focal length f_1 creates an image at a distance of i_1. This can be seen as an object at distance

$$o_2 = l_2 - i_1 = f_1 + f_2 - i_1 \tag{4.2}$$

before the second lens which creates an image at a distance of i_2 after the second lens, with l_2 being the distance of both lenses, idealized as $f_1 + f_2$. This implies $i_1 \leq l_2$. The thin lens formula then gives:

$$i_2 = \frac{1}{\frac{1}{f_2} - \frac{1}{f_1+f_2-\frac{1}{\frac{1}{f_1}-\frac{1}{o_1}}}}\,. \tag{4.3}$$

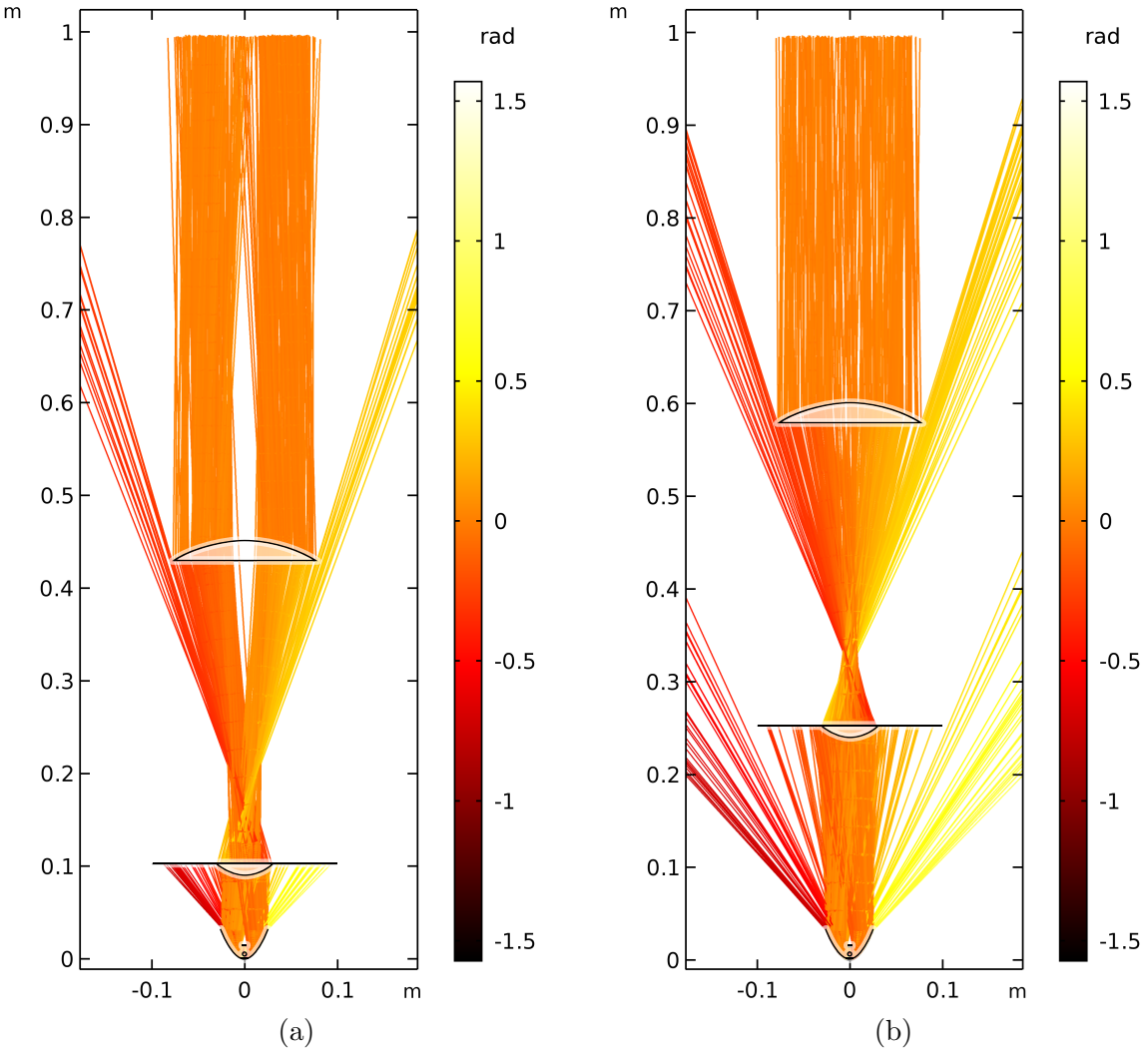

Figure 4.5: Ray trajectories plot for distances l_1 of 50 mm and 200 mm. Lens parameters are: $d_1 = 60\,\text{mm}$, $d_2 = 155\,\text{mm}$, $f_1 = 80\,\text{mm}$, $r_2/r_1 = 180/50.8$, the second lens is moved 30 mm out of focus. The simulation is 2d axisymmetric. 500 rays are shown. The plots are rendered with COMSOL and edited for a highlighted geometry of the optical system. Rays beside the first lens are dumped as only the part of the beam is regarded, that passes every optical component.

If o_2 is smaller than f_2, the thin lens equation for the second lens leads to a negative value of i_2. The image is therefore only virtual and not imaged in this case. This can be restated:

$$o_2 < f_2 \text{ — use equation (4.2)} \tag{4.4}$$

$$\Leftrightarrow f_1 < i_1 \text{ — use thin lens formula for first lens} \tag{4.5}$$

$$\Leftrightarrow 1 < \frac{1}{1 - \frac{f_1}{o_1}} \tag{4.6}$$

For $o_1 > f_1$ this relation is true and therefore only a virtual image of the object exists. For $o_1 < f_1$, the relation equation (4.6) is false and therefore the object is imaged.

Hence, the low radiation zone only appears if the shadow is visible in the ray bundle within a distance of the focal length before the first lens. By comparing intensity distribution plots, one finds that in a distance of 30 mm to the parabolic mirror the shadow cannot be seen anymore. In the setup considered from now on, a distance l_1 of 0.2 m between mirror and lens is used, as it is enough even for large focal lengths of the first lens up to 170 mm, which has been proved by intensity plots for all focal lengths discussed in the following.

4.3 Lens diameters

In the following subsections the diameters of both lenses are derived.

For choosing the diameter of the first lens, two constraints have to be considered: The smaller it is, the less rays pass it, which reduces the intensity and the beam diameter. The larger it is, the more diverging rays are collected and most importantly its spherical aberration rises. None of these constraints depend on the actual lens geometry or a lens specific optical effect. Hence, for optimization of this parameter, the integral plot for a cut at the position of the first lens can be used. As the divergence causes the beam diameter to rise with propagation time, optimization for an l_1 of 0.2 m gives an upper limit for the diameter of the first lens. The corresponding plot can be seen in figure 4.6. This plot shows a high amount of rays (64461 of 83964 $\hat{=}$ 76.8 %) inside a diameter of 60 mm which will therefore be used for further simulations.

The diameter of the second lens may not be larger than 155 mm because of environmental confinements. It is has to widen the rays to a spatially constant distribution as the rear wall is tilted to the optical axis and hence spatial inconstancy is directly reflected in the homogeneity of its illumination. The illumination should not deviate over 10 % within a diameter of 140 mm, which causes the diameter of the second lens to be at least 140 mm. The diameter of the second lens can therefore be varied in the following optimizations between

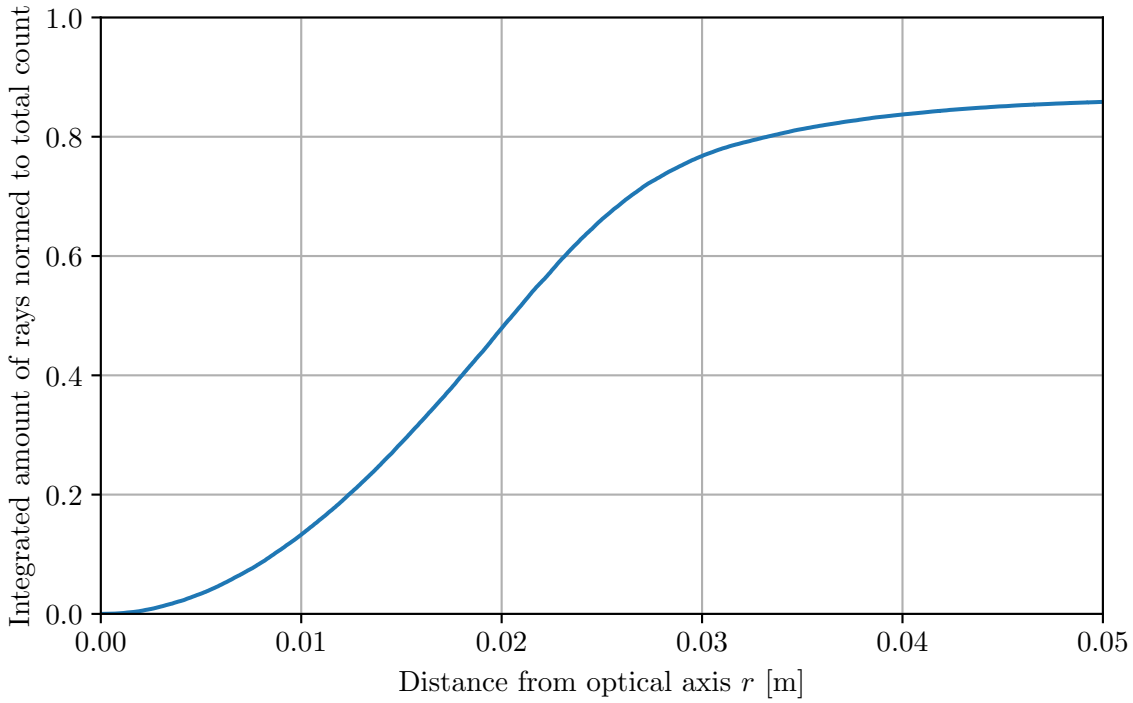

Figure 4.6: Integration plot for a cut plane distance to the parabolic mirrors aperture of 200 mm. Only lamp components were simulated

140 mm and 155 mm. A diameter of 140 mm causes inhomogeneities at the outer part of the ray bundle over the spatial propagation at least for a lens setup in which both lenses are perfectly positioned in the common focus. This is discussed in section 4.4. An explanation is given by the divergence of the rays inside the ray bundle. While their divergence can at least partly be compensated inside because of different propagation directions, the divergence of the outer rays is not compensated at all. The only possible drawback of a large second lens is its spherical aberration which is discussed below.

4.4 Spherical aberrations

One limiting factor in the lenses' size and the homogeneity of the rear wall illumination is the spherical aberration. For a diameter of the first lens of 60 mm and a diameter of the second lens of 155 mm, the spherical aberration is plotted for different focal lengths. The plot for $f_1 = 60\,\text{mm}$, shown in figure 4.7, shows a strong increase of the spherical aberration for larger distances from the optical axis. This can be reduced by increasing f_1. For the second lens with a diameter of 155 mm, as shown in figure 4.8, the reduction of the spherical aberration for the edge of the beam is not that high for the plotted focal lengths, although the spherical aberration in the beams middle is larger.

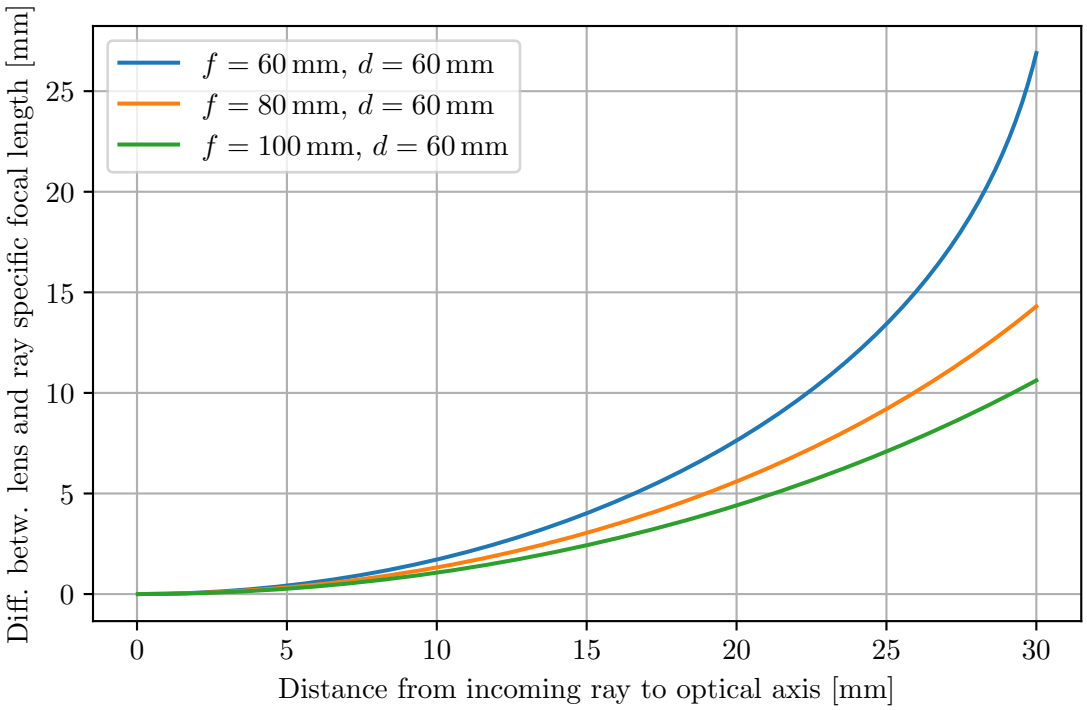

Figure 4.7: Spherical aberration calculated as presented in section 3.3 for a lens diameter of 60 mm and focal lengths of 60, 80 and 100 mm.

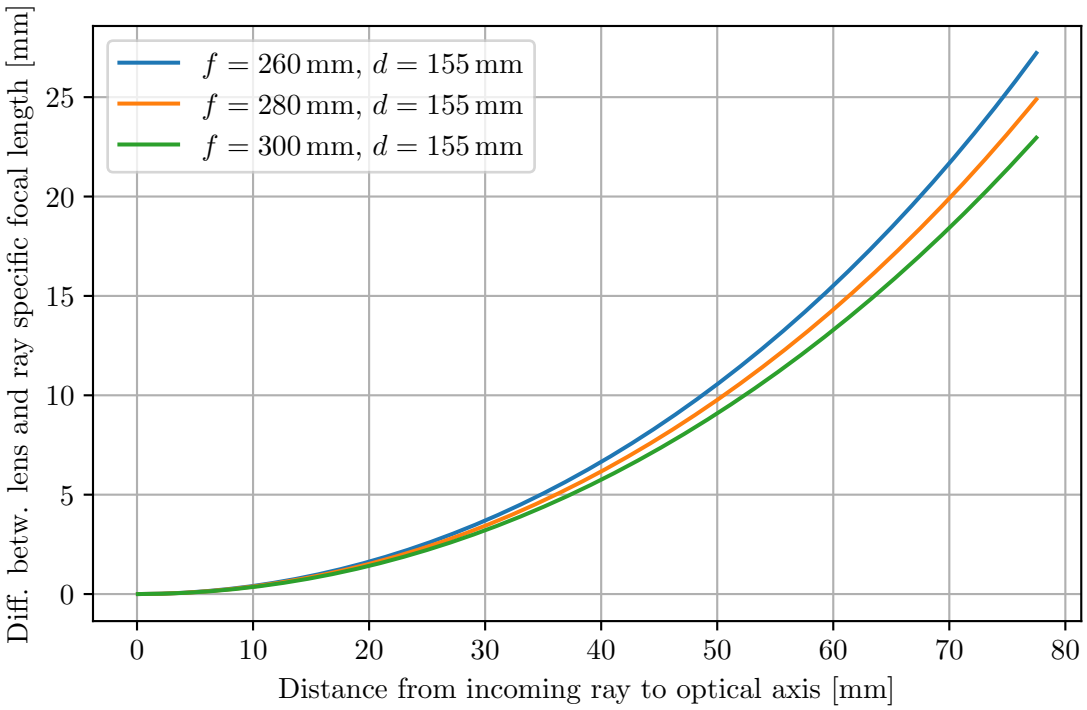

Figure 4.8: Spherical aberration calculated as presented in section 3.3 for a lens diameter of 155 mm and focal lengths of 260, 280 and 300 mm.

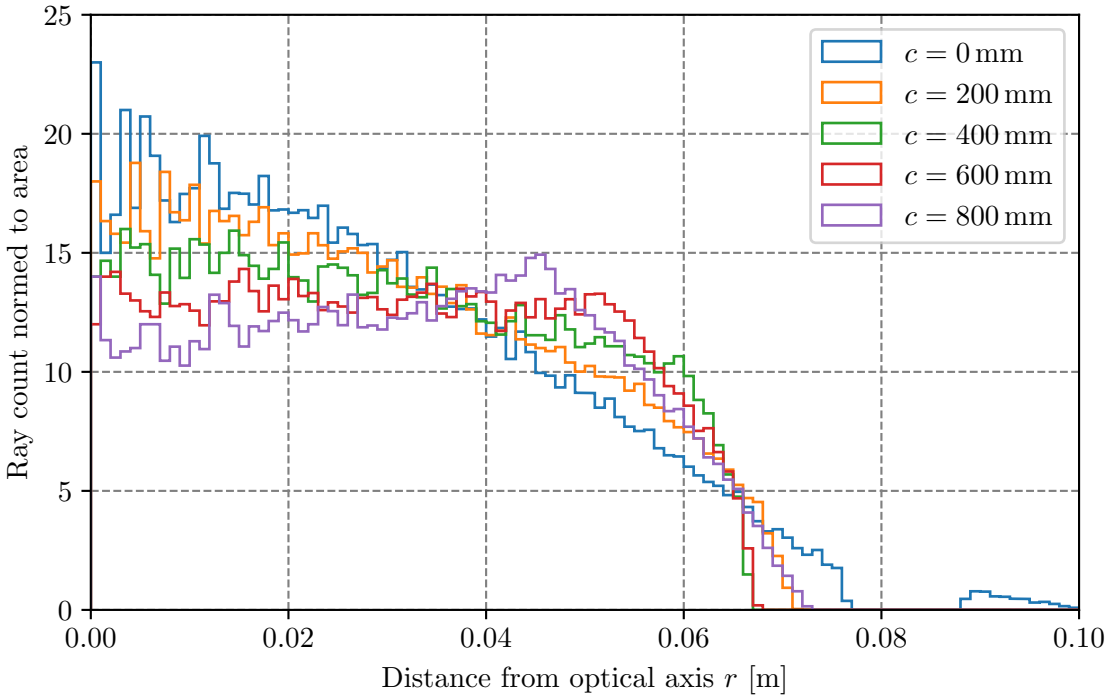

Figure 4.9: Intensity distribution plot for distances c of 0, 200, 400, 600 and 800 mm between second lens and cut plane. Lens setup: As presented, $d_1 = 60\,\mathrm{mm}$, $d_2 = 155\,\mathrm{mm}$ $f_1 = 100\,\mathrm{mm}$.

In these plots, the distance is measured towards the lens. As the shown distances are positive, the spherical aberration causes the effective focal length for rays at the edge of the beam to be shorter than the calculated focal length.

The plots also verify the formula used to calculate principal plane positions as it is used to determine the focal points and the plots show that for small distances from the optical axis, the ray-specific focal lenght adheres to the lenses theoretical focal length.

4.5 Distance between lenses

The lamp specifies $2 \cdot r_1$ to be 50.8 mm and $2 \cdot r_2$ is at least 140 mm. With this optical expansion set, as long as the lenses stay in focus, their focal lengths only depend on each other as stated in equation (2.1). For f_2 this results in:

$$f_2 = f_1 \cdot \frac{r_2}{r_1}\,. \tag{4.7}$$

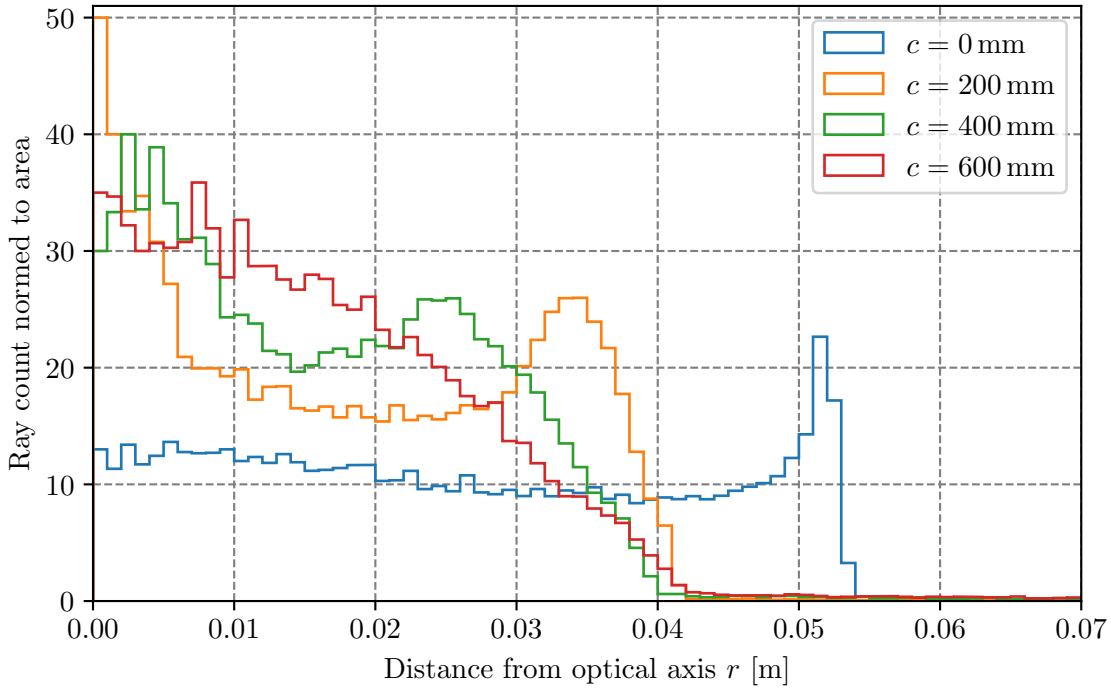

Figure 4.10: Intensity distribution plot for distances c of 0, 200, 400 and 600 mm between second lens and cut plane. Lens setup: As presented, $d_1 = 60\,\mathrm{mm}$, $d_2 = 155\,\mathrm{mm}$ $f_1 = 57.3\,\mathrm{mm}$.

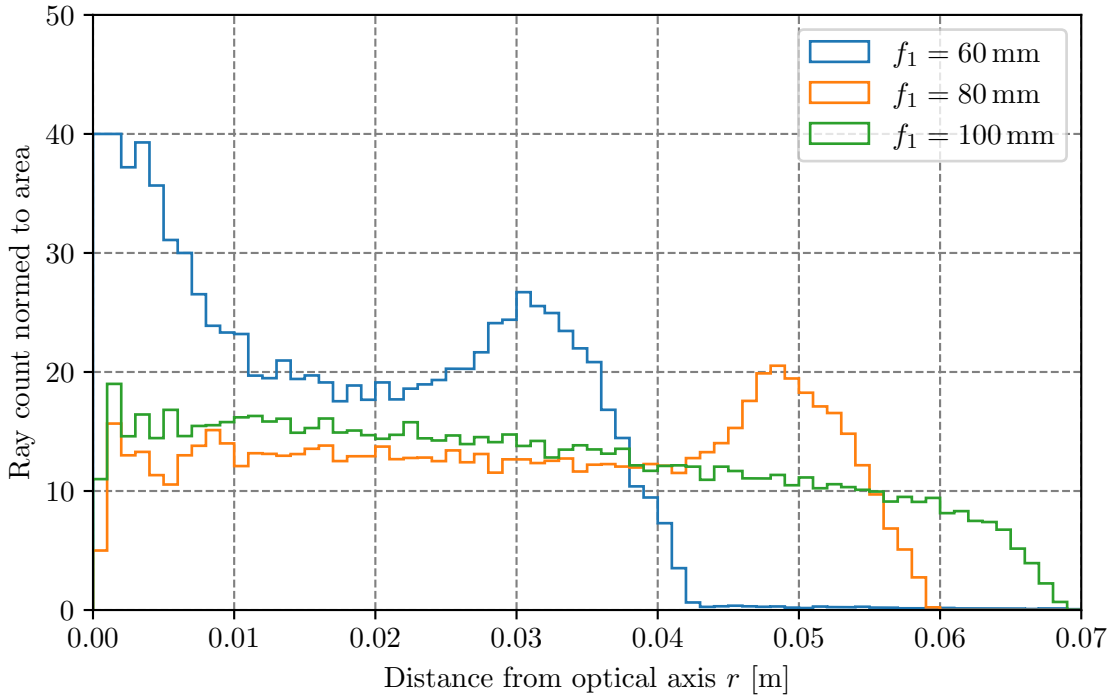

Figure 4.11: Intensity distribution plot with f_1 of 60, 80 and 100 mm with a cut distance of 300 mm between second lens and cut plane. Lens setup: As presented, $d_1 = 60\,\mathrm{mm}$, $d_2 = 155\,\mathrm{mm}$.

For $f_1 = 100\,\text{mm}$, this leads to in the distribution shown in figure 4.9 for cuts 0, 200, 400, 600 and 800 mm behind the second lens. It can be seen that the outer ray divergence causes a considerable inhomogenity.

As the first lens has a diameter of 60 mm, its maximum radius of curvature is 30 mm as lenses with a smaller radius of curvature must have a smaller diameter. For rays with a wavelength of 225 nm this gives a minimal focal length of the first lens of approx. 57.3 mm and therefore a distance of both lenses of approx. 190.9 mm. This is the smallest focal length of the first lens, so the lens has its maximal thickness and therefore a high spherical aberration, which results in the inhomogenity visible in figure 4.10. This illustrates the problem of too small focal lengths resulting from small distances between both lenses. In comparison with figure 4.9 it can be seen that the spherical aberration antagonizes the dispersion of outer rays caused by the divergence of the Cermax lamp, while it introduces a new divergence. While the simulation with minimal f_1 shows too much spherical aberration, for $f_1 = 100\,\text{mm}$ the uncompensated divergence of the lamp comes to fore. Therefore, in the following, values for f_1 between 60 and 100 mm are considered. As the comparison of results for f_1 of 60, 80 and 100 mm in cuts 300 m behind the second lens in figure 4.11 shows, every distribution has a drastical falloff before it reaches the desired diameter of 140 mm. It will now be discussed how this divergence can be compensated.

4.6 Divergence compensation

It is shown that, although this telescope setting should widen the ray to a diameter of 140 mm, the intensity drops already at a lower diameter. It has also been seen that this is caused by two sources of divergence, the extended emitter geometry and the lense's spherical aberration. While the first type of divergence only blurs the beam geometry, the second type causes the rays at the beams edges to propagate towards the optical axis. To solve this problem, the second lens can be defocused and the expansion of the lens system can be enlarged.

4.6.1 Defocusing second lens

Defocusing the second lens can be done by either scaling its focal length or by moving the second lens. As established in section 4.4, the rays at the beam's edge "feel" a smaller focal length of both lenses. Therefore the second lens is too far away to collect the rays at the desired distance. As the focal length of the second lens is already scaled in the previous

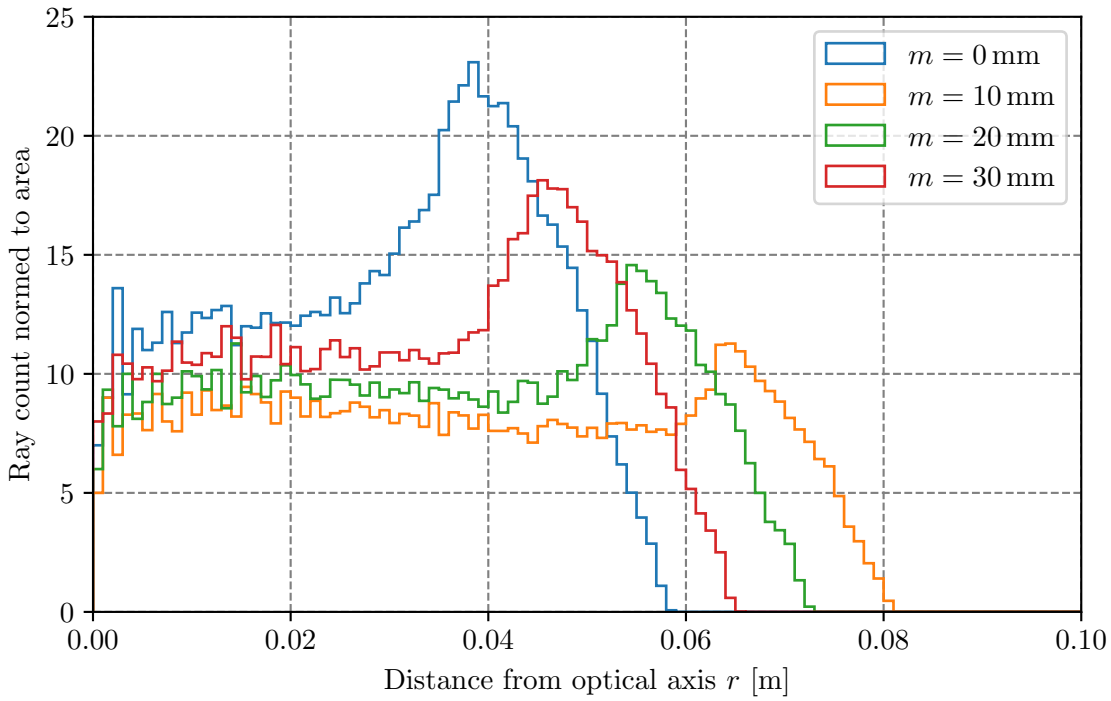

Figure 4.12: Intensity distribution plot for cuts at a constant distance to the second lens of 0.5 m with the second lens moved 0, 10, 20 and 30 mm closer to the first lens than in the initial setup.

subsection and the fundamental problem is the spherical aberration that can be compensated by moving the second lens, in the following this is done to accomplish a homogeneous emission.

By moving the second lens from its position in the initial setup 0, 10, 20 and 30 mm closer to the first lens, calling this variable of defocusion m, one gets the intensity plots shown in figure 4.12. These plots show the spherical aberration as discussed in section 4.4. To reduce this inhomogenity, a second solution to the compensation of the divergence has to be discussed.

4.6.2 Wider expansion

The spherical aberration of the first lens can be compensated by widening the beam with the telescope setup to larger diameters. Therefore some of the outer rays do not reach the second lens. If the beam is widened carefully and the amount of lost rays is acceptable, this reduces the peak at the borders resulting from the spherical aberration fully as it can be seen for $m = 20\,\mathrm{mm}$ in figure 4.13. For $f_1 = 80\,\mathrm{mm}$ this results in $r_2 = 180\,\mathrm{mm}$ at which the peak of intensity from outer rays is neglectable. This value of r_2 can be used in a variation plot for

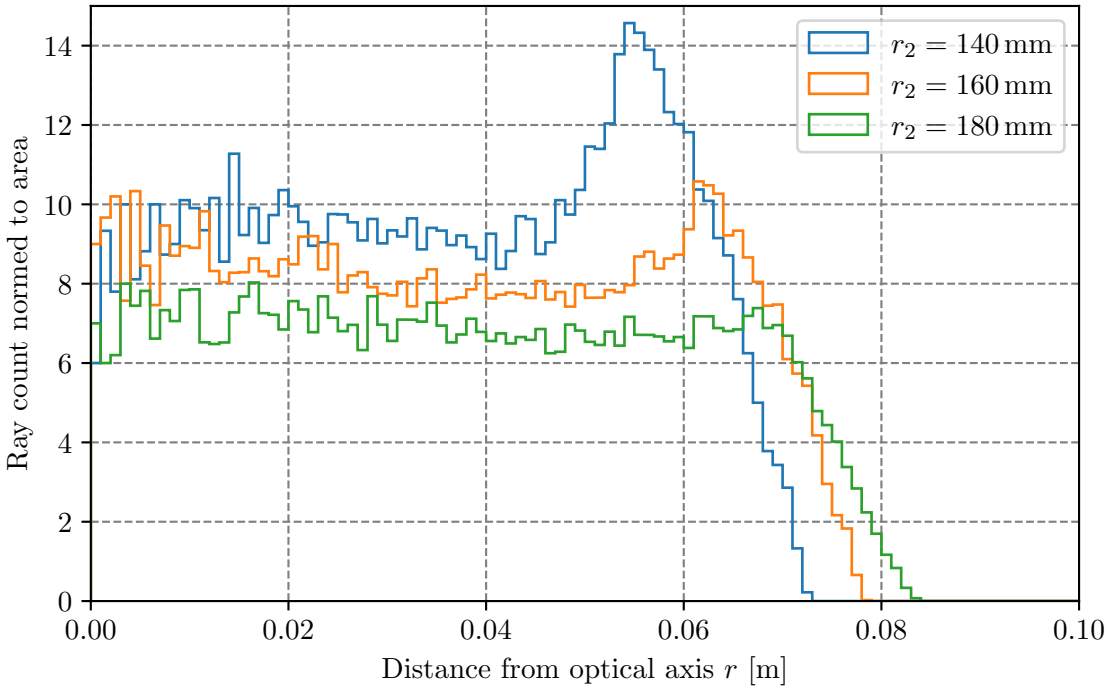

Figure 4.13: Intensity distribution plot for cuts with varied r_2 of 140, 160 and 180 mm at a constant distance to the second lens of 0.5 m with $m = 20\,\mathrm{mm}$.

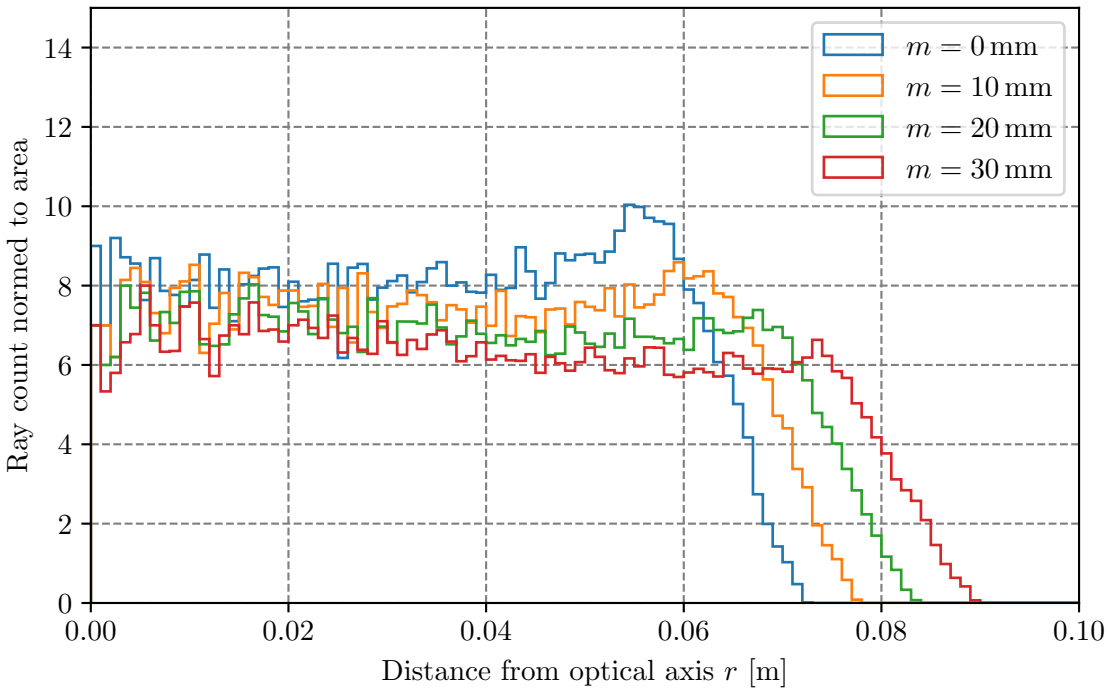

Figure 4.14: Intensity distribution plot for cuts at a constant distance to the second lens of 0.5 m with the second lens moved 0, 10, 20 and 30 mm closer to the first lens than in the initial setup with a beam expansion of $r_2/r_1 = 180/50.8$.

Table 4.1: Final lens geometry. All values are given in mm. Values annotated with ^{d} are set by constraints to other parameters.

	First lens	Second lens
Focal length $f_{1/2}$	80	283.5^d
Diameter $d_{1/2}$	60	155
Distance of primary plane to planar face $c_{1/2}$	8.3^d	14.3^d
Thickness	12.7^d	21.8^d

m again, which is done in figure 4.14. For $m = 20\,\text{mm}$, the remaining spherical aberration peak is at a comparable height to the intensity in the beam middle.

The presented variations have been done multiple times for different values until $f_1 = 80\,\text{mm}$ was chosen. Therefore $m = 20\,\text{mm}$, $r_2/r_1 = 180/50.8$ and the resulting lens parameters determine the final lens configuration, as it can be found in table 4.1.

4.7 Result characterization

In this section properties of the final lens geometry are identified. Beginning with an analysis of the homogeneity, for three wavelengths the intensity distribution is discussed and compared. This is followed by a calculation of the overall intensity on the rear wall.

4.7.1 Homogeneity

The intensity shall not to vary over the rear wall in more than a 10 % confidence interval. As the minimal illuminated diameter of the rear wall in both width and height is 140 mm and the rear wall is rotated in one direction as seen in figure 2.4, the distance c between the plane of the second lens and the rear wall is not constant, but varies with the rear wall position. For a rear wall at an average distance of 500 mm, this gives a distance range of $(500 \pm 70 \cdot \cos(54°))\,\text{mm}$, which corresponds to approx. 459 to 541 mm. In figure 4.15, the intensity distribution is shown for cuts at these distances. It can be seen that except for known small statistical outliers at small distances from the optical axis, all values lie inside the marked confidence interval of 10 %.

In figure 4.16, the intensity distribution for a wavelength of 200 nm is plotted. It shows a drastical elevation of the beam intensity at the beam border and the beam falls off before the rear wall diameter is reached. As common dichroic mirrors with edges at the desired wavelength of approx. 260 nm, such as Semrock Di01-R266, have a low reflectance for wavelengths near 200 nm [20], and the intensity distribution of the Cermax lamp has a low output at this wavelength, this inhomogeneity can be neglected.

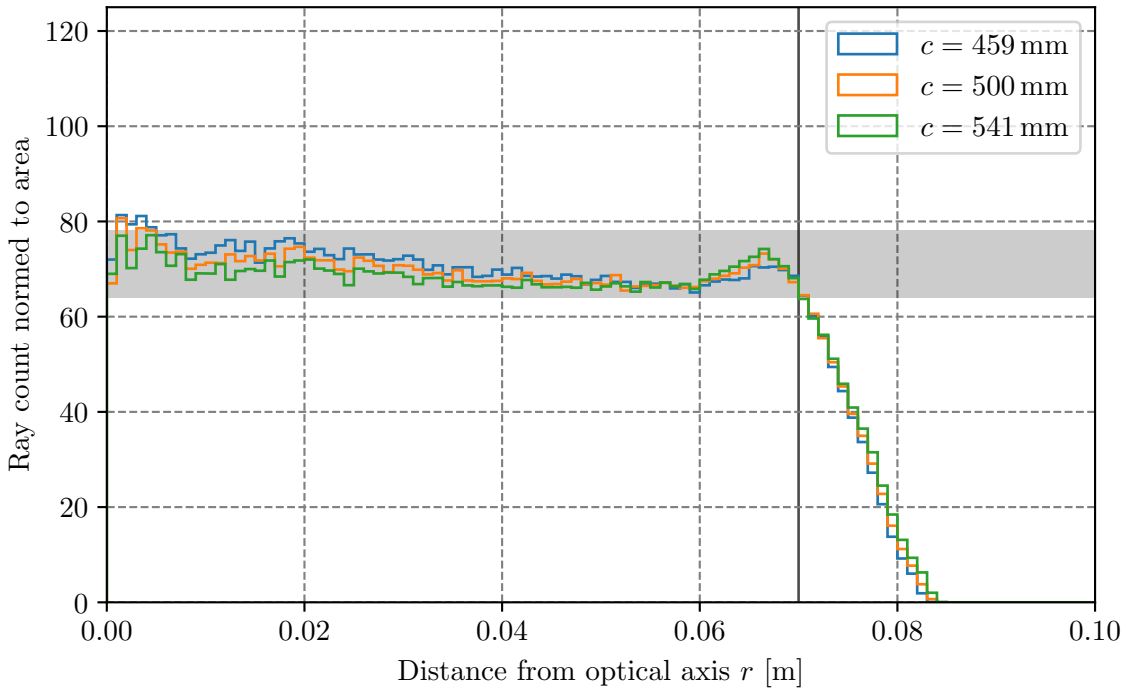

Figure 4.15: Intensity distribution cuts for a simulation with wavelength of 225 nm at a distance c of 459, 500 and 541 mm behind the second lens. The gray area surrounds a 10 % confidence interval around a normed intensity count of 71, the black line marks the desired rear wall illumination diameter of 140 mm. For this simulation, the final setting described in section 4.6 is used. Simulated with 10^6 rays.

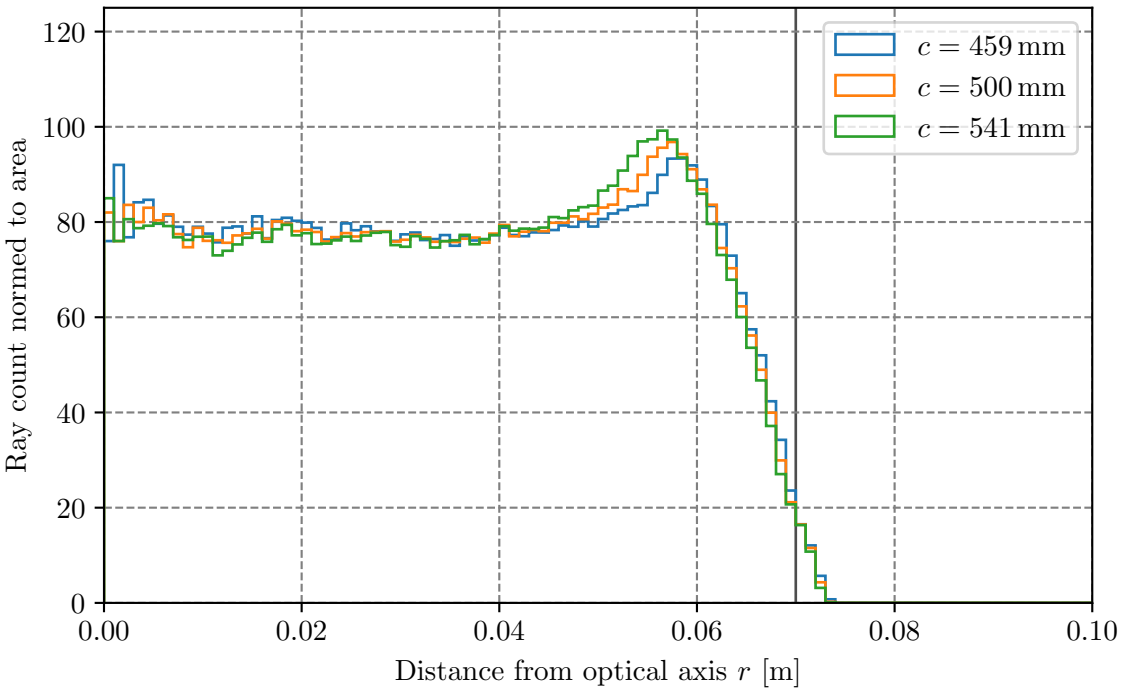

Figure 4.16: Intensity distribution cuts for a simulation with wavelength of 200 nm at a distance c of 400, 500 and 600 mm behind the second lens. For this simulation, the final setting described in section 4.6 is used. Simulated with 10^6 rays.

However, the inhomogeneity of rays at 260 nm cannot be neglected, as figure 4.17 shows. It can be enclosed, as done with the cuts shown in figure 4.15 with a confidence interval of at least 16 %. Some values of the cut for $c = 400\,\mathrm{mm}$ and a distance from the optical axis smaller than 10 mm lie outside the interval. Because near the optical axis the rear wall has a distance of around 500 mm to the second lens, the large values for the cut at a distance of $c = 400\,\mathrm{mm}$ can be neglected.

4.7.2 Intensity

The intensity at the rear wall is calculated by counting the rays that reach a simulated, circular rear wall with a diameter of 140 mm at a distance of 0.5 m behind the second lens. 255920 out of 835795 rays ($\approx 30.62\,\%$) exiting the lamp hit the rear wall. The lamp emits, as in section 2.1 derived, a power of approx. 1.74 W for rays between 200 and 260 nm and a power of approx. 2.10 W for rays between 200 and 266 nm. Multiplied by the calculated factor of rays reaching the rear wall, this gives an estimated power of 0.53 W for wavelengths between 200 and 260 nm and 0.64 W for wavelengths between 200 and 266 nm, which is more than the specified minimal rear wall illumination power of 0.2 W.

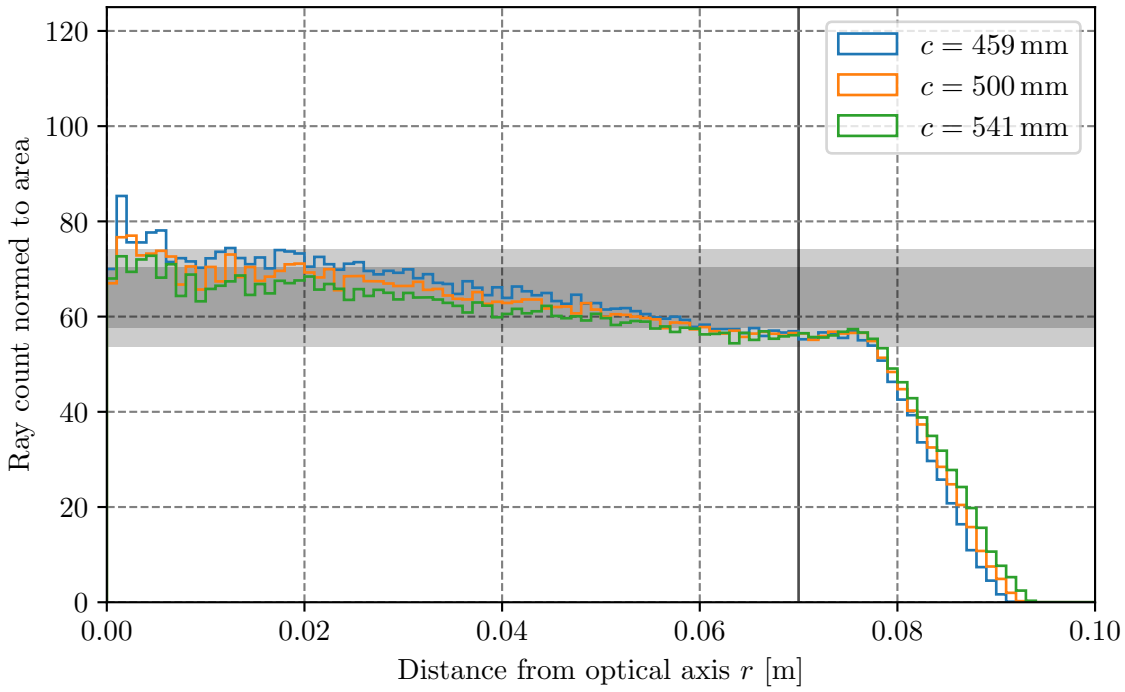

Figure 4.17: Intensity distribution cuts for a simulation with wavelength of 260 nm at a distance c of 459, 500 and 541 mm behind the second lens. The light gray area marks a 16 % confidence interval whereas the dark gray area surrounds a 10 % confidence interval around a normed intensity count of 64, the black line marks the desired rear wall illumination diameter of 140 mm. The black line marks the desired rear wall illumination diameter of 140 mm. For this simulation, the final setting described in section 4.6 is used. Simulated with 10^6 rays.

5 Conclusion and outlook

In this thesis, the constraints and relations of the optical system's parameters have been discussed with the use of divers ray tracing simulations. Therefore the lamp and lens geometry have been implemented in COMSOL. For the lamp, multiple assumptions had to be made, including the emitter size and distribution and the inner structure of the lamp. To approximate the source, a 3d Gaussian distribution with $\sigma = 0.5\,\text{mm}$ was choosen. Anode and cathode of the lamp were idealized as two planar, circular blinds with position and diameter estimated from a technical drawing. Due to the fact that every simulation was performed with a monochromatic emitter, the dichroic mirrors were neglected for this simulation. After a discussion on the different plot types used in this thesis and the differences between 2d and 3d simulations, the simulation results were presented and discussed.

First, the inhomogeneity of the ray bundle emitted by the lamp was examinated using three different emitter sizes: Point source, $\sigma = 0.1\,\text{mm}$ and $0.5\,\text{mm}$ for a Gaussian distributed source. It has been found that the beam geometry is closely linked to the emitter size. As the arc widens over time, a larger ray source than specified was chosen.

After the initial beam geometry was set, the effects of the lamp's internal blinds on the ray trajectories, namely the effective imaging of the blinds, were inspected. A theoretical description of this effect was derived and the resulting rule to avoid this imaging was applied. This resulted in a set value of the distance between parabolic mirror and first lens of $l_1 = 200\,\text{mm}$.

In the next step, the geometry of the first lens was determined. The amount of light collected by a lens with a diameter of $d_1 = 60\,\text{mm}$ turned out to be sufficient with $76.8\,\%$ of 83964 rays passing the respective area with the given diameter. Therefore, this diameter was used in the further analysis. The focal length of the first lens determines the focal lenght and position of the second lens and therefore had multiple implications for the lenses' spherical aberration that had to be considered. Therefore, the diameter of the second lens was considered first. This diameter has to be between 140 and $155\,\text{mm}$. As it had to be compensated, that the lamp does not emit parallel rays, the larger diameter of $155\,\text{mm}$ was chosen.

After discussing the effect of enlarging the beam expansion and defocusing of the second lens using simulations with a diameter of 80 mm, the optimal setting for this diameter has been found to be an expansion of $r_2/r_1 = 180/50.8$ and a reduction of the distance of both lenses of 20 mm. The focal length of the first lens of 80 mm is already the result of an optimization process, therefore this configuration is the final configuration proposed in this thesis.

Then, homogeneity and intensity of the radiation of this setup were analyzed. The desired homogeneity inside a confidence interval of 10 % could be reached for the wavelength of 225 nm used for the optimization process. For short wavelengths, the homogeneity does not meet the demands, but this is unproblematic since the illumination power of these wavelengths is very small. For high wavelengths of around 260 nm, the homogeneity lies inside a maximal interval of 16 %. The rear wall is illuminated with an intensity of est. 0.53 W with wavelengths between 200 and 260 nm, which is larger than the demanded value of 0.2 W. This allows later masking and e.g. an even wider expansion. As this intensity is calculated without considering losses on lenses and mirrors and for a single wavelength of 225 nm, this intensity is only an upper guide value and has to be precised in future simulations. As this thesis covered plano-convex spherical lenses, a further examination of e.g. biconvex and aspheric lenses can lead to an illumination with an even better homogeneity.

For a following successful realization of the optical system, the real intensity distribution of the Cermax lamp in different distances from the lamp has to be measured for different burning times. With this information, the simulation can be further enhanced. Furthermore, the real wavelength distribution can be implemented to predict the intensity distribution more precisely. By performing these additional improvements, the optical illumination at the rear wall could not only be enhanced but also precisely characterized.

Bibliography

[1] Kerstin Schoenung. "Development of a rear wall for the KATRIN rear section and investigation of tritium compatibility of rear section components". [Online, accessed 16.11.2017]. PhD thesis. Jan. 2016. URL: https://publikationen.bibliothek.kit.edu/1000056077/3861598 (cit. on p. 2).

[2] S. Mertens. *Background Processes in the Electrostatic Spectrometers of the KATRIN Experiment*. Springer Theses. Springer International Publishing, 2013. ISBN: 9783319011776. URL: https://books.google.de/books?id=hgK7BAAAQBAJ (cit. on p. 1).

[3] Nicholas Steinbrink et al. "Neutrino mass sensitivity by MAC-E-Filter based time-of-flight spectroscopy with the example of KATRIN". In: (2013). DOI: 10.1088/1367-2630/15/11/113020. arXiv: 1308.0532. URL: https://arxiv.org/pdf/1308.0532.pdf (cit. on p. 1).

[4] NA Titov. "Sensitivity and systematics of KATRIN experiment". In: *Physics of Atomic Nuclei* 67.11 (2004), pp. 1953–1958. URL: http://www.inr.ru/~trdat/papers/phan1953.pdf (cit. on p. 2).

[5] Florian Habermehl. "Electromagnetic measurements with the KATRIN pre-spectrometer". In: (2009). URL: https://publikationen.bibliothek.kit.edu/1000013549 (cit. on p. 2).

[6] B. Monreal & M. Beck KATRIN rear section working group et al. *KATRIN Rear Section Technical Design Report 2012*. Apr. 2012 (cit. on p. 2).

[7] Laura Kuckert. "The Windowless Gaseous Tritium Source of the KATRIN Experiment-Characterisation of Gas Dynamical and Plasma Properties". PhD thesis. Dissertation, Karlsruhe, Karlsruher Institut für Technologie (KIT), 2016 (cit. on p. 2).

[8] Excelitas Technologies Corp. *Cermax® Products and Specifications*. [Online; accessed 14.11.2017]. 2011. URL: http://www.excelitas.com/downloads/dts_cermaxproductsandspecifications.pdf (cit. on pp. 3, 6, 10, 11).

[9] Excelitas Technologies Corp. *Cermax® Xenon Lamp Engineering Guide*. [Online; accessed 15.11.2017]. 2011. URL: http://excelitas.com/Downloads/Cermax_Eng_Guide.pdf (cit. on pp. 5, 11, 19).

[10] William Cassarly. “Taming light”. In: *OE magazine* (Dec. 2002), pp. 16–18 (cit. on p. 4).

[11] R John Koshel. *Illumination Engineering: design with nonimaging optics*. John Wiley & Sons, 2012, pp. 31–33 (cit. on p. 4).

[12] Eugene Hecht. “Optik, 4., überarbeitete Auflage”. In: *Wien-München: Oldenbourg* (2005) (cit. on pp. 6, 20).

[13] Carl R. Nave. *Principal Planes*. [Online, accessed 15.11.2017]. URL: http://hyperphysics.phy-astr.gsu.edu/hbase/geoopt/priplan.html (cit. on p. 6).

[14] COMSOL AB. *COMSOL Multiphysics®, ver. 5.3*. https://www.comsol.com. 2017 (cit. on p. 9).

[15] Python Software Foundation. *Python Language Reference, version 3.6.1*. [Online; accessed 12.11.2017]. 1991–2017. URL: https://www.python.org/ (cit. on p. 9).

[16] Eric Jones, Travis Oliphant, Pearu Peterson, et al. *SciPy: Open source scientific tools for Python*. [Online; accessed 12.11.2017]. 2001–2017. URL: http://www.scipy.org/ (cit. on p. 9).

[17] Prof. Howard E. Haber. *Focusing properties of spherical and parabolic mirrors, Physics 5B*. [Online; accessed 15.11.2017]. 2009. URL: http://scipp.ucsc.edu/~haber/ph5B/parabolic09.pdf (cit. on p. 12).

[18] L. H. Malitson. “Interspecimen Comparison of the Refractive Index of Fused Silica”. In: *Journal of the Optical Society of America (1917-1983)* 55 (Oct. 1965), p. 1205 (cit. on p. 13).

[19] ISP Optics Corporation. *Fused Silica UV Grade (SiO2)*. [Online; accessed 14.11.2017]. Feb. 2015. URL: http://store.ispoptics.com/Content/Images/uploaded/MP%20SiO2%20uv.pdf (cit. on p. 13).

[20] Used MyLight-Tool on page; [Online, accessed 22.11.2017]. URL: https://www.semrock.com/filterdetails.aspx?id=di01-r266-25x36 (cit. on p. 30).